Bulletin of the Seismological Society of America, Vol. 84, No. 3, pp. 780–791, June 1994

Postseismic Deformation Following the Landers Earthquake, California, 28 June 1992

by Zheng-Kang Shen, David D. Jackson, Yanjie Feng, Michael Cline, Mercedes Kim, Peng Fang, and Yehuda Bock

Abstract Accelerated strain followed the Landers and Big Bear earthquakes, returning to the normal rate only after a period of several months. We observed this strain throughout most of southern California using the Global Positioning System (GPS). Three GPS receivers operating continuously in fixed positions at Pinyon Flat, Jet Propulsion Laboratory (Pasadena), and Goldstone all recorded postseismic deformation in a relative sense. In addition, we established 16 sites where we deployed portable receivers occasionally over a period of about 6 months near the rupture zones of the earthquakes. Anomalous postseismic displacements ranged from 55 mm near the epicenter to a few millimeters far from the fault. We modeled the displacements, using dislocation theory, as due to variable slip on the faults that were displaced at the times of the earthquakes. The model suggests that the postseismic strain released the equivalent of about 15% of the seismic moment of the mainshock. While the strain released from the upper 10 km is about the same as what can be explained by direct effects of aftershocks, the major contribution of strain release comes from the lower layer, below 10-km depth. Significant afterslip or viscous relaxation must have occurred below 10-km depth to explain the observed deformation more than 100 km from the fault. One interpretation is that high stress on the margin of the co-seismic rupture zone drives the rupture to extend itself into unbroken rock below and along the initial rupture zone.

Introduction

The 28 June 1992 Landers earthquake (*M* 7.5) and its *M* 6.6 Big Bear aftershock provide a unique opportunity to study the rheological behavior of the crust in a rupture zone. The surface rupture of the earthquake is about 85-km long, and the maximum dislocation of the fault is greater than 6 m (Sieh *et al.*, 1993; Hart *et al.*, 1993). Earthquakes of such magnitude are likely to excite significant postseismic deformation, owing to viscous response of the crust and upper mantle to a sudden stress change. There have been numerous reports of geodetic postseismic deformations in the past. Significant elevation changes were found after the 1946 Nankaido *M* 8.2 earthquake (Okada and Nagata, 1953; Fitch and Scholz, 1971). Deformations were also noticed more than 20 yr after the 1959 Hebgen Lake *M* 7.5 earthquake (Reilinger, 1986), and several years after the 1984 Morgan Hill *M* 6.4 earthquake (Savage *et al.*, 1987). In California, strain rates near the San Andreas fault apparently decay exponentially with time following large earthquakes (Thatcher, 1983). Near Landers, geodetic measurements during the 1.9 yr following the 1979 Homestead *M* 5.6 earthquake revealed noticeable postseismic deformation, equivalent to about 10% of the co-seismic deformation (Stein and Lisowski, 1983). However, all the previous studies were limited by the scope of the available geodetic data. Coverage was generally inadequate both spatially and temporally. In responding to the Landers earthquake, we measured the crustal deformation using the Global Positioning System (GPS). This space geodetic technique allows us to survey a fairly dense network and to achieve unprecedented accuracy of postseismic deformation measurements for further studies.

Data

Our GPS field observations started within 36 hr following the Landers earthquake. During the first round of the experiment, which lasted 3 weeks, more than 20 stations were occupied using Trimble 4000SST and Ashtech LX-II receivers. The GPS data were collected for 24 hr for each session at most of the sites. Durations of the station occupations varied from 1 day at several sites

Table 1
Station List

Site	Designation	Stamping	Latitude	Longitude
6052	6052	T5N R4E SECS 13 14 23 24	N34°30′58″	W116°50′25″
7000	7000	GLO T7N R3E 1919	N34°40′35″	W116°42′57″
7001	7001	GLO T6N R5E 1919	N34°33′36″	W116°28′09″
BEAR	BIG BEAR	BIG BEAR	N34°15′51″	W116°53′03″
BLAC	BLACK BUTTE NCMN 7269	BLACK BUTTE NCMN 1982	N33°39′49″	W115°43′11″
CABA	CABAZON	(3D unstamped)	N33°54′57″	W116°46′32″
GARN	GARNET	GARNET 1979	N33°53′52″	W116°32′16″
GODW	GODWIN	GODWIN 1965	N34°08′11″	W115°55′54″
HECT	HECTOR 2	HECTOR 2 1966	N34°47′06″	W116°25′14″
LAZY	LAZY	LAZY 1980	N34°20′38″	W116°30′50″
ONYX	ONYX	ONYX 1939 1982	N34°11′33″	W116°42′34″
PAXU	PAX NCER	PAX NCER 1977	N34°09′12″	W116°23′23″
SAND	DEADMAN LAKE–SAND HILL 7267	SAND HILL 1939 1987	N34°15′18″	W116°16′44″
SOAP	HPGN CA 08 04	HPGN 08-4 GPS-SOAP 1990	N34°54′14″	W116°58′51″
VIEW	VIEW 2	VIEW 2 1986	N33°55′35″	W116°11′16″
WIDE	WIDEVIEW	WIDE (3D)	N33°55′53″	W116°24′23″
DS10	GOLDSTONE	(PGGA permanent site)	N35°25′31″	W116°53′21″
JPL1	JPL MESA	(PGGA permanent site)	N34°12′17″	W118°10′24″
PIN1	PINYON FLAT	(PGGA permanent site number 1)	N33°36′44″	W116°27′29″

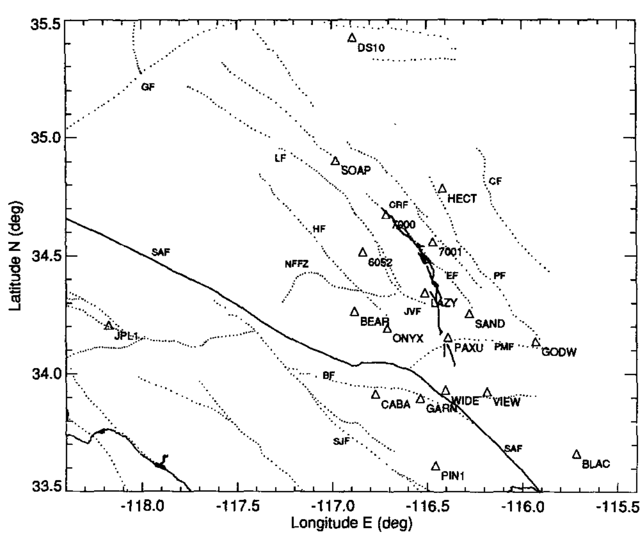

Figure 1. Map of the surface rupture of the Landers earthquake (thick curves, from digitized maps by Sieh *et al.*, 1993). Dotted lines are the following faults in southern California; BF, Banning fault; CF, Calico fault; CRF, Camp Rock fault; EF, Emerson fault; GF, Garlock fault; HF, Helendale fault; JVF, Johnson Valley fault; LF, Lenwood fault; NFFZ, Northern Frontal Fault Zone; PF, Pisgah fault; PMF, Pinto Mountain fault; SAF, San Andreas fault; and SJF, San Jacinto fault. The triangles are the stations of the GPS postseismic monitoring network.

to 3 weeks of continuous observations at two portable sites. Some of the sites were revisited for 2 to 4 days during September and October 1992 using Trimble 400SST receivers. A complete reoccupation using Ashtech LX-II, Trimble 4000SST, and Trimble 4000SSE P-code receivers was conducted 5 to 6 months after the earthquake in November and December 1992. At that period, 6 hr of data were collected during the time of best satellite coverage. We select 16 local stations (Table 1 lists the four-digit site identifiers, site names, stampings, and coordinates) with good occupation history covering the 6 month time period. Figure 1 shows the network configuration and the trace of the surface breaks of the earthquake. Occupation history is listed in Table 2. This data set, together with three southern California Permanent GPS Geodetic Array (PGGA) stations located at Goldstone (Mojave), JPL (Pasadena), and Pinyon Flat (Riverside County), spans nearly the entire co-seismic rupture area of the Landers and the Big Bear earthquakes.

GPS Data Processing

We use the GAMIT software (King and Bock, 1993) to process the data. Although the data were collected with a 30-sec sampling interval in general, they are decimated to 120-sec sampling to save computation time. We process the data from the global tracking network of the International GPS Service for Geodynamics (IGS) (Beutler and Brockmann, 1993) along with our local data to solve for the satellite orbits simultaneously. Positions of the fiducial tracking stations are constrained to ITRF91 coordinates, which were derived from a combination of Very Long Baseline Interferometry (VLBI), Satellite Laser Ranging (SLR), Lunar Laser Ranging (LLR), and GPS coordinate solutions (IERS, 1992). In the daily solution processing, we first make station clock corrections to the phase data using pseudo-range measurements. Then we use the dual frequency, double-differenced phase measurements to form LC (ionosphere-free) combinations, and fit the data by the least-squares method. We solve for the local station positions, along with tropospheric delay residuals, integer-cycle phase ambiguities, and satellite orbital parameters. We round the ambiguities to integer values when a certain confidence limit is reached (Dong and Bock, 1989). Ten millimeters of uncertainty is assumed for the phase data. For further details about the processing method, see Bock *et al.* (1986), Schaffrin

Table 2
Local Station Observation History

JDAY	6052	7000	7001	BEAR	BLAC	CABA	GARN	GODW	HECT	LAZY	ONYX	PAXU	SAND	SOAP	VIEW	WIDE
92/181									•	•		•	•		•	•
92/182							•		•	•		•	•		•	•
92/183							•	•	•	•		•	•		•	•
92/184		•		•	•		•		•			•	•	•	•	•
92/185	•	•		•	•	•	•			•		•		•		•
92/186	•	•	•	•	•	•	•			•		•				•
92/187		•	•	•	•	•	•			•		•				•
92/188					•	•	•				•	•				•
92/189			•			•				•	•	•				•
92/190				•		•				•		•				•
92/191		•	•	•		•	•			•		•				•
92/192		•	•	•			•			•		•				
92/193		•	•	•			•					•				
92/194		•	•	•			•			•		•				
92/195				•			•			•		•	•			
92/196				•								•	•			
92/197				•								•	•			
92/198				•								•				
92/199				•								•				
92/200				•								•				
92/201				•								•				
92/202				•								•				
92/204					•											
92/205					•											
92/206					•											
92/207					•											
92/251		•		•			•									
92/252		•	•	•			•									
92/253	•			•							•					
92/254									•	•	•	•				
92/255						•				•		•				
92/275		•	•													•
92/276		•	•													•
92/317				•		•				•	•			•		
92/318				•							•					
92/323					•			•								
92/324					•			•								
92/325									•							
92/328	•	•	•				•		•	•		•	•	•		•
92/329								•					•			
92/337		•				•						•				
92/338			•													
92/339	•						•								•	•
92/356							•									•
92/357							•									•
93/013	•														•	•

and Bock (1988), Dong and Bock (1989), Feigl (1991), and Feigl *et al.* (1993). Samples of daily baseline solutions are displayed in Figure 2. The error bars of the daily baselines are one standard deviation.

Station Displacement Modeling

Our measurements give us the relative positions (i.e., vector baselines) between pairs of survey markers at selected times. We fit these data to a model in which each survey marker is moving with a time-dependent vector velocity, with the time dependence having a simplified functional form. Estimating the station velocities is a generalized form of geodetic adjustment.

From the time sequences of the baselines illustrated in Figure 2, it is clear that most of the sites have moved since the earthquake. What kind of relaxation function best explains the data? Among the simple models to describe rheological behavior of rocks, the following three are commonly used: exponential, logarithmic, and power

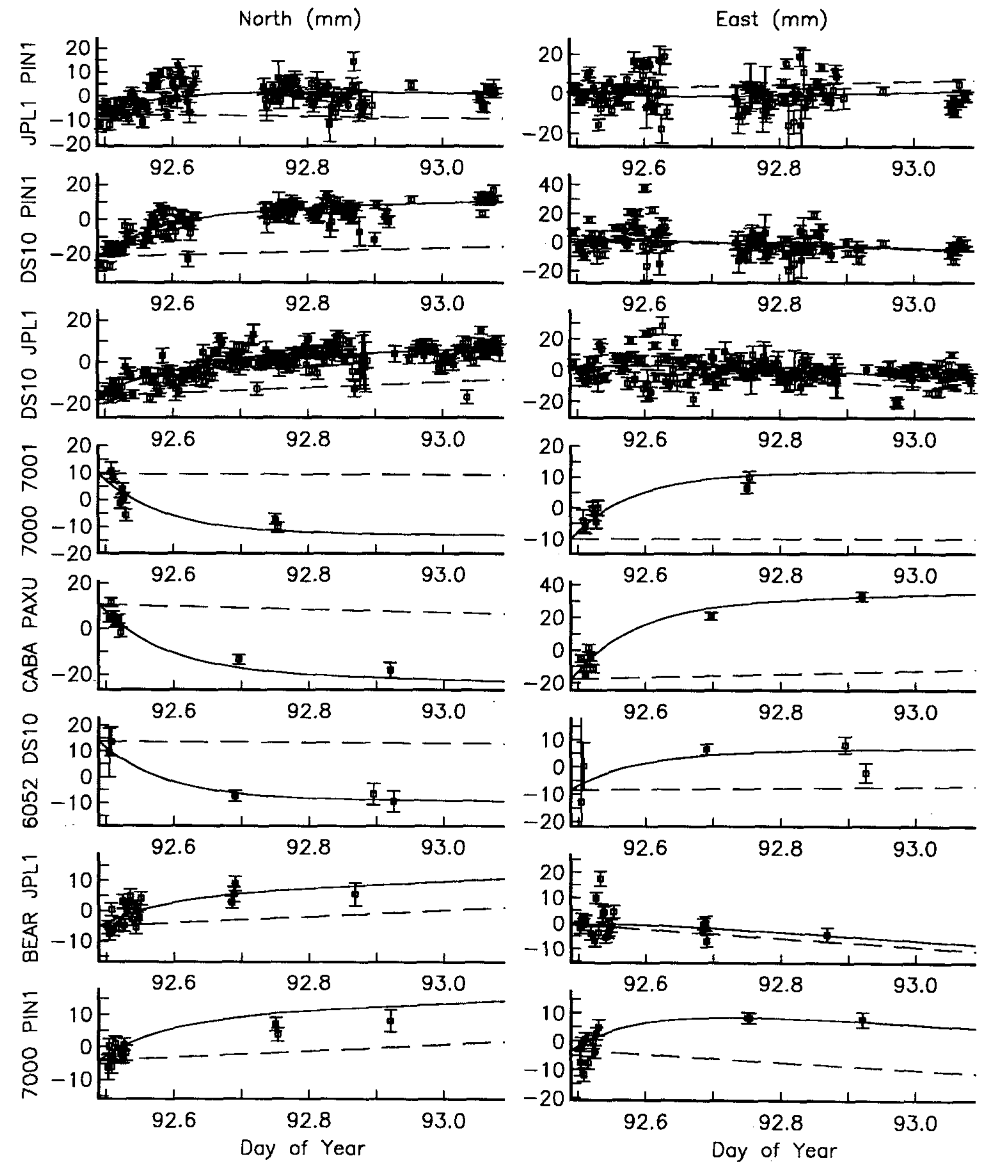

Figure 2. Examples of the daily GPS baseline solutions, two horizontal components versus time. Figures start at the time of the Landers earthquake. Relaxation is significant for most of the baselines. The dashed curves are linear secular baseline changes predicted by a dislocation model of Hirata *et al.* (unpublished manuscript). The solid curves are the secular baseline changes, plus the baseline changes derived from the station displacements predicted by an exponential relaxation model (τ_e = 34 days) obtained by adjusting the baseline data.

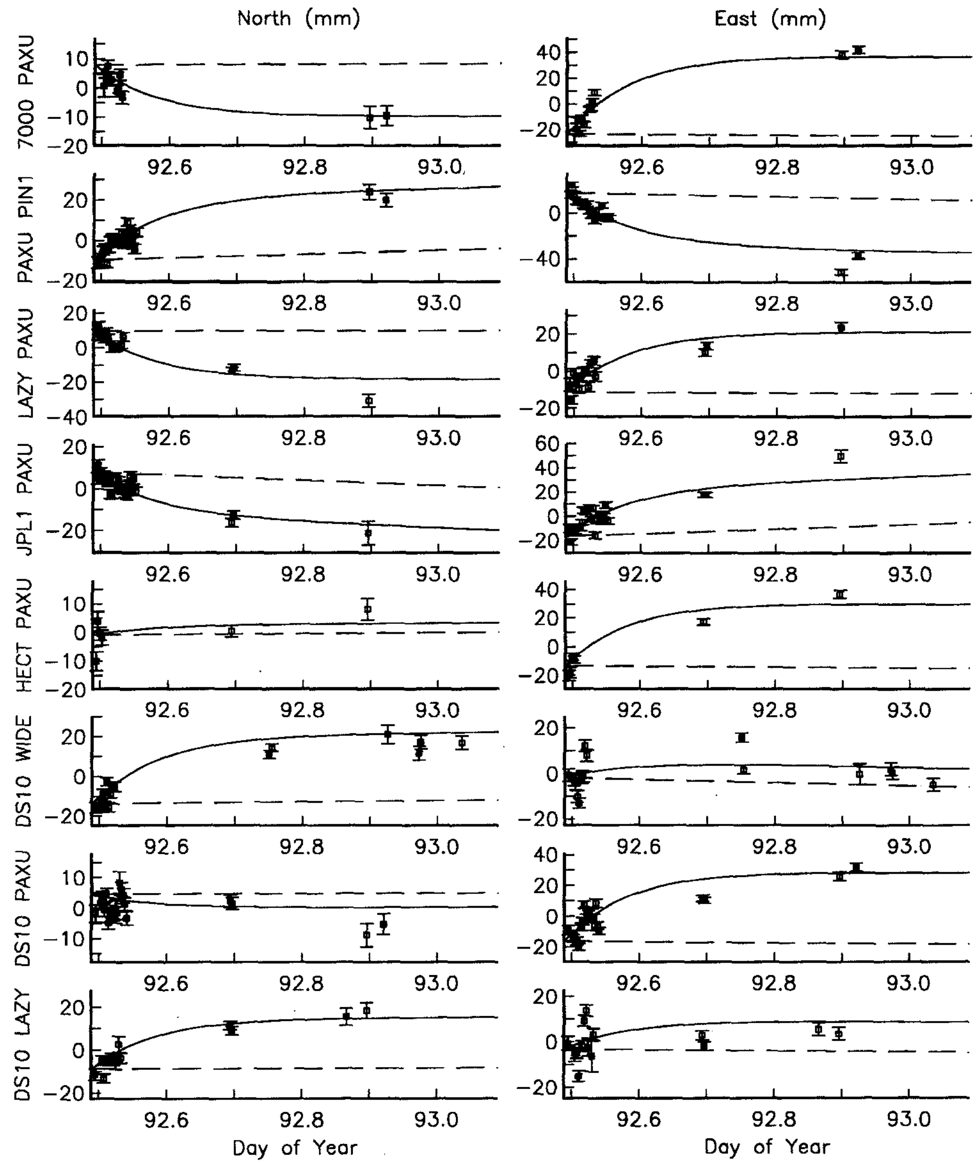

Figure 2—*Continued*

law (Jaeger and Cook, 1979). Each of the models has its advantages for describing viscous deformation. Maxwell solids, which are idealized viscoelastic materials, exhibit exponential relaxation. However, many rock mechanics experiments are best described by logarithmic relaxation. The power-law relaxation can be related to aftershock seismicity. Omori's law of aftershocks gives (Reasenberg and Jones, 1989)

$$n(t, M) \propto t^{-p} f(M),$$

where $n(t, M)$ is the earthquake rate at time t and magnitude M after the mainshock, p is the power-law index, and $f(M)$ is a function of aftershock magnitudes. The postseismic deformation resulting from aftershocks should be proportional to the integration of $n(t, M)$ over time and earthquake magnitude. If the ratio of seismic to aseismic moment release does not vary much with time, we should have for the relaxation displacement $D(t)$,

$$D(t) \propto \begin{cases} \ln t, & \text{if } p = 1; \\ t^{1-p}, & \text{otherwise.} \end{cases}$$

We explore the validity of using all three models to fit our data. Daily relative baseline vector solutions are used as input. Only horizontal components are modeled; vertical components are excluded because of their large uncertainties. For a baseline from station i to station j, we have

$$L_{ij}(t) = P_j(t) - P_i(t).$$

For a logarithmic relaxation,

$$P(t) = P(t_{eq}) + D \log \left(1 + \frac{t - t_{eq}}{\tau_l}\right) + V(t - t_{eq}) + \epsilon;$$

for an exponential relaxation,

$$P(t) = P(t_{eq}) + D \left[1 - \exp\left(-\frac{t - t_{eq}}{\tau_e}\right)\right] + V(t - t_{eq}) + \epsilon;$$

and for a power-law relaxation,

$$P(t) = P(t_{eq}) + D \left(\frac{t - t_{eq}}{\tau_p}\right)^{1-p} + V(t - t_{eq}) + \epsilon;$$

where τ_l and τ_e are the relaxation time constants for logarithmic and exponential models, respectively. The $P(t_{eq})$ and D are the unknowns for the station position directly after the earthquake and the amplitude of relaxation, respectively. The term τ_p is a time constant, p is the power-law index, and V is a constant station velocity, reflecting secular steady motion of the station. Station velocity V is given by a *a priori* information, computed from a California velocity model by Hirata *et al.* (unpublished manuscript) This model interprets GPS, VLBI, triangulation, and trilateration observations in California using a block-fault model, with slip along faults and rotations and translations of blocks between the faults. The aseismic *a priori* relative station velocities are listed in Table 3, along with the station displacement vectors solved using exponential relaxation.

We estimate the relaxation constant (τ_l or τ_e) or index p, and unknowns $P(t_{eq})$ and D, in two steps. First, we select the baselines from a group of five stations, DS10, JPL1, PIN1, LAZY, and PAXU. Those stations span a relatively long time period (6 months) and show clear relaxation. We make consecutive least-squares adjustments of the data, each time assuming a relaxation constant or index number. The best estimate of the relaxation constant or index number is the one with the least χ^2 of the postfit residuals. An F test is applied to estimate the confidence intervals of the relaxation constants. The exponential relaxation time τ_e is estimated at 34 days (15 days $< \tau_e <$ 150 days at 70% confidence level). The logarithmic relaxation time τ_l is about 4 days, where $\tau_l <$ 50 days at 70% confidence. The power-law index p is best estimated at 0.79, where $0.34 < p < 1.13$ at 70% confidence. The three models fit the data almost equally well. Second, having obtained the best estimate of the relaxation constant, we then fix the constant to the best estimated value and do the least-squares adjustment for all 19 stations. The exponential relaxation model is used to obtain the solutions. The amplitudes D of the station relaxation are shown in Figure 3, with sta-

Table 3
Station Relaxation Displacements with Respect to PIN1

	Adjusted D*			Predicted D†		*A Priori* Secular V‡	
Site	East (mm)	North (mm)	Corr.	East (mm)	North (mm)	East (mm/yr)	North (mm/yr)
6052	−14.7 ± 7.6	−3.8 ± 4.9	−0.22	−5.5	−7.0	12.0	−8.8
7000	−16.1 ± 2.0	−12.8 ± 2.0	−0.07	−14.4	−7.8	13.3	−10.0
7001	5.6 ± 2.4	−35.0 ± 2.5	−0.05	6.1	−32.2	13.3	−10.4
BLAC	10.4 ± 3.9	−10.2 ± 4.3	−0.06	1.6	−14.5	9.1	−7.1
BEAR	3.1 ± 2.3	−20.1 ± 2.3	−0.10	5.6	−15.6	10.5	−7.9
CABA	−1.1 ± 2.6	−1.2 ± 2.8	−0.12	2.2	3.1	1.1	−2.4
DS10	−0.8 ± 1.7	−26.0 ± 1.6	−0.08	−1.4	−21.9	14.1	−10.1
GARN	10.6 ± 2.1	3.4 ± 2.2	−0.08	5.8	6.1	4.3	−4.1
GODW	22.7 ± 3.8	−9.3 ± 4.5	−0.11	12.1	−17.3	12.2	−9.9
HECT	0.7 ± 2.7	−34.1 ± 2.9	−0.06	1.5	−31.5	13.9	−10.7
JPL1	5.6 ± 1.7	−10.4 ± 1.6	−0.10	−0.3	−12.6	−8.0	3.3
LAZY	12.3 ± 2.1	−2.6 ± 2.3	−0.08	10.3	2.6	12.0	−9.5
ONYX	−2.4 ± 3.6	−3.0 ± 3.8	−0.16	2.2	0.7	9.3	−7.4
PAXU	45.5 ± 2.1	−30.7 ± 2.2	−0.08	44.4	−28.5	10.8	−9.2
SAND	9.9 ± 2.7	−42.1 ± 3.2	−0.07	6.9	−27.0	12.0	−10.1
SOAP	−0.5 ± 3.3	−3.1 ± 3.6	−0.08	−0.6	4.3	13.8	−9.7
VIEW	6.3 ± 2.4	−20.0 ± 2.6	−0.11	14.3	−20.8	9.5	−8.2
WIDE	7.1 ± 1.8	7.8 ± 1.9	−0.07	9.5	6.7	7.2	−6.3

*Adjusted D: adjusted station displacement vectors as a result of relaxation.
†Predicted D: model predicted station displacement vectors as a result of relaxation.
‡*A Priori* Secular V: *a priori* secular station velocities.

tion PIN1 fixed as a reference. The selection of the reference station is somewhat arbitrary, since all the displacements derived here are relative. Station PIN1 is chosen only for better visualization of relative motions among stations west of the main rupture zone. Comparison of the postseismic relaxation with the co-seismic displacements shows a similar displacement pattern, except that the postseismic amplitudes are much smaller and the contrast between postseismic near-field displacements and far-field displacements is not as large. This observation motivates the attempt to map the station relaxations directly to the fault patches in the vicinity of the co-seismic rupture.

Fault Relaxation Modeling

There are generally two kinds of physical models to explain postseismic relaxation. In one model, viscoelastic relaxation is assumed to occur throughout the volume of the crust and upper mantle at a rate dependent on the rheology and on the local stress (Nur and Mavko, 1974; Li and Rice, 1987). In another model, displacements are assumed to result from "afterslip" or continued slip on the fault planes ruptured in the earthquake (Tse and Rice, 1986). Rundle and Jackson (1977) (also Savage and Prescott, 1978; Thatcher, 1983; Savage, 1990) showed that the two models are essentially indistinguishable since they predict very similar surface deformation. Here we adopt the afterslip model for computational convenience, recognizing that the modeled postseismic slip may occur throughout a volume surrounding the fault, rather than strictly on the fault plane.

To model the postseismic deformation along faults, we first need to locate the fault planes. The surface rupture during the mainshock may not reflect all the sources of postseismic deformation, because some faults activated by the main event may not have surface expression. The aftershock seismicity following the Landers/Big Bear events allows us to find the faults which were seismically activated by the main event. The faults in our model are the ones clustered in the mainshock and aftershock regions: Camp Rock, Emerson, Landers, Johnson Valley, Eureka Peak, and Joshua Tree, plus the Big Bear fault, Barstow aftershock zone, Pisgah fault, two east–west aftershock lobes east of the Camp Rock fault, and the Banning fault (see Hauksson *et al.*, 1993; Kanamori *et al.*, 1992; Hart *et al.*, 1993).

We divide the faults into patches, shown in Figure 4. Uniform slip is assumed on each patch. Station position changes are described by

$$D_i = \sum_j \frac{\partial P_i}{\partial U_j} U_j + \epsilon_i,$$

where U_j is the horizontal slip at the jth patch and ϵ_i is the error of the station displacement D_i. We use the dislocation model of Matsu'ura *et al.* (1986) to propagate fault dislocation U to station position change D. An elas-

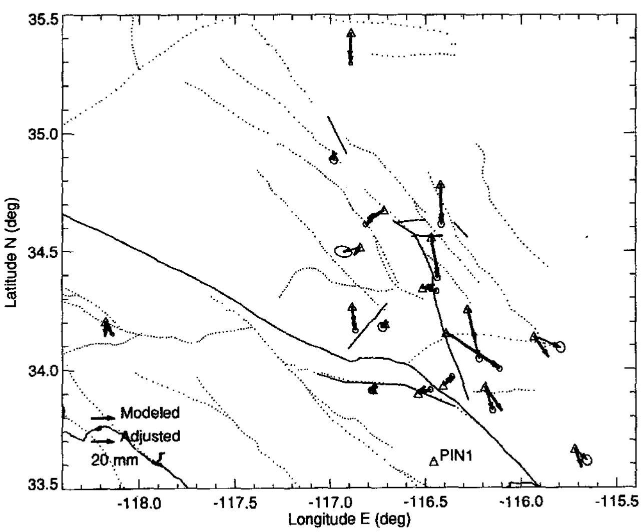

Figure 3. Station relaxation amplitudes by adjustment and by prediction from model A. Solid lines are the fault patches in the model. Arrows with an error ellipse are from the adjustment; thick arrows without an ellipse are predicted from model A. Error ellipses are one standard deviation. Good agreement between the two suggests that the postseismic deformation in the rupture zone can be explained by afterslip along the fault surfaces, at and beneath the seismogenic zone.

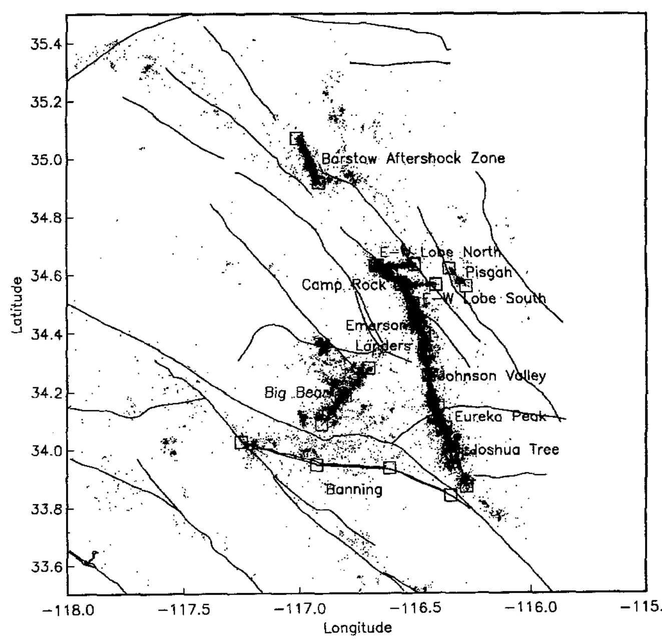

Figure 4. Fault model for postseismic slips. The dots show aftershock seismicity. Open squares denote the nodal points of the fault patches.

tic half-space is assumed for the model. Only horizontal slip is allowed along the faults. The locations and the upper and lower bounds of the fault patches are given *a priori*, except during some test runs described later.

Our starting model has two layers. The first layer, 0 to 10 km in depth, represents the elastic crust, part of which ruptured during the Landers/Big Bear earthquakes. The second layer, 10 to 35 km in depth, is probably the main source of the postseismic deformation, since the far-field displacements are relatively large. In order to avoid extreme discontinuities of deformation along the faults caused by sparsity of the data, an *a priori* smoothing constraint is introduced. For each laterally and vertically adjacent fault pair i and j, we constrain dislocations,

$$D_i - D_j = 0 \pm 70 \text{ mm}.$$

A Bayesian inversion method is applied (Jackson, 1979; Jackson and Matsu'ura, 1985). Since smoothing is achieved at the expense of increasing the observational residual χ^2, the uncertainty of the *a priori* constraints is selected between trade-offs that the reduced data residual χ^2 is not too much higher than unity and that the slip directions along the patches do not violate much of what we know about the overall strain orientation in the region. The solutions are given in model A (Table 4 and Fig. 5).

To account for the number of data, we have 18 independent relative baselines, which give 36 data points. Although 33 fault patches are included in the model, the actual number of degrees of freedom in model space is significantly reduced because of the *a priori* smoothing constraints imposed on the model. Table 4 lists the diagonal elements of the resolution matrix; these measure the degree to which displacement on each fault patch is resolved by the geodetic data (Jackson and Matsu'ura, 1985). The total resolution of model A is 17.2. In general, the fault patches in the upper layer are resolved better than the ones in the lower layer. We prefer to em-

Table 4
Solution of Model A

Fault Patch	Slip* (mm)	t-Value	Resolution (%)	Moment (10^{17} N-m)
Upper Barstow	45 ± 26	1.8	88	2.6
Upper Camp Rock	64 ± 48	1.3	60	2.3
Upper Emerson W	31 ± 54	0.6	20	0.8
Upper Emerson E	18 ± 30	0.6	62	0.7
Upper Landers	15 ± 35	0.4	64	0.3
Upper Johnson V N	−76 ± 27	−2.8	79	−1.7
Upper Johnson V S	123 ± 11	11.7	95	5.3
Upper Eureka Pk	−7 ± 12	−0.6	95	−0.2
Upper Joshua Tr N	64 ± 25	2.6	78	2.2
Upper Joshua Tr S	−10 ± 22	−0.5	86	−0.4
Upper E–W Lobe N	−101 ± 38	−2.6	63	−4.1
Upper E–W Lobe S	25 ± 28	0.9	79	1.0
Upper Pisgah	57 ± 92	0.6	49	1.6
Upper Big Bear S	−70 ± 32	−2.2	71	−3.0
Upper Big Bear N	49 ± 25	2.0	83	2.1
Lower Barstow	249 ± 53	4.7	67	36.0
Lower Camp Rock	33 ± 69	0.5	24	3.0
Lower Emerson W	41 ± 64	0.6	10	2.8
Lower Emerson E	55 ± 58	1.0	15	5.0
Lower Landers	26 ± 61	0.4	11	1.3
Lower Johnson V N	25 ± 58	0.4	13	1.4
Lower Johnson V S	120 ± 50	2.4	30	13.0
Lower Eureka Pk	156 ± 50	3.1	24	10.3
Lower Joshua Tr N	150 ± 49	3.1	27	12.9
Lower Joshua Tr S	55 ± 50	1.1	48	5.3
Lower E–W Lobe N	−102 ± 55	−1.8	39	−11.3
Lower E–W Lobe S	−51 ± 62	−0.8	28	−5.2
Lower Pisgah	60 ± 90	0.7	52	4.2
Lower Big Bear S	−96 ± 55	−1.7	35	−10.3
Lower Big Bear N	−63 ± 51	−1.2	48	−6.8
Lower Banning E	−39 ± 33	−1.2	84	−7.8
Lower Banning C	119 ± 37	3.2	68	25.9
Lower Banning W	100 ± 86	1.2	29	10.4

*Minus sign indicates left-lateral slip.

phasize the regionalized patterns averaged over more than one fault patch rather than the individual solutions.

We test several other models against model A. model B tests the significance of the Barstow fault zone; model C, two east–west lobes of the aftershocks; model D, the Pisgah fault; model E, the San Bernardino Mountain section of the San Andreas fault (SBM–SAF); model F, the Banning fault; and model G and H test separately the inclusion of dislocations at two seismic gaps. One of the gaps extends from the northern tip of the Camp Rock aftershock zone to the southern tip of the Barstow aftershock zone (Barstow gap), and the other extends from the northeastern tip of the Big Bear aftershock zone to intercept the Camp Rock–Emerson fault (Big Bear gap).

Results (Table 5) show that our inclusion of the Barstow patch is significant at 99% confidence. Inclusion of the two east–west aftershock lobes is significant at 90% confidence. Inclusion of the Pisgah fault is not statistically significant. The Barstow gap favors a slight left-lateral slip, and the Big Bear gap favors a slight right-lateral slip, but both are inconsistent with the regional stress pattern and are not statistically significant. The Banning fault is significant at 84% confidence. Inclusion of the San Bernardino Mountains segment of the San Andreas fault results in slight left-lateral motion of the fault, which is not statistically significant. We also test the exclusions of the lower layer and the upper layer in models I and J. Both layers are significant at 99% confidence, indicating that both layers have important contributions to the postseismic deformation.

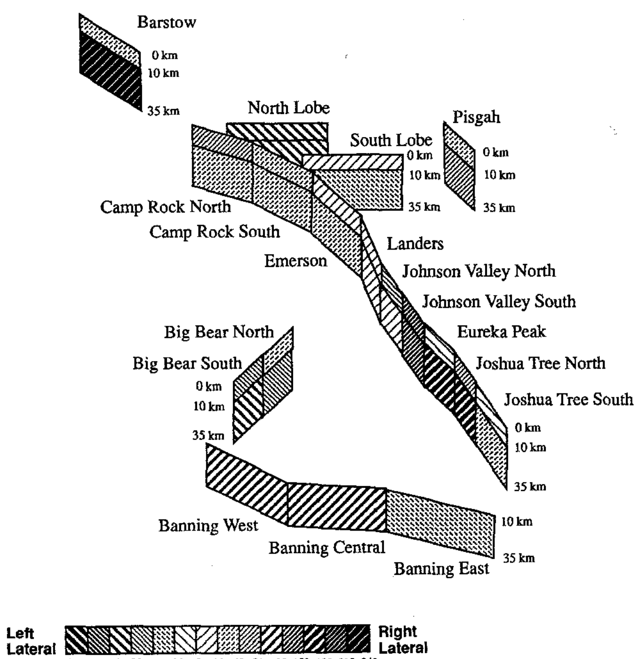

Figure 5. Results from model A. Significant postseismic slip is found along the Barstow aftershock zone, the southern patch of the Johnson Valley fault, the Eureka Peak fault, and the northern patch of the Joshua Tree fault.

Although model A is the best we can derive from the data, it is by no means a unique model, being but one among many possible models. What is important in this model is that by using minimal *a priori* constraints, we find that the postseismic deformation can be attributed to afterslip along faults ruptured during the mainshock, along with those below and at the edges of the main rupture faults and some nearby faults activated by the mainshock.

Discussion

We estimate the exponential relaxation time τ_e to be about 34 days. Wdowinski *et al.* (1992), using the PGGA sites only, detected significant displacements involving PIN1 and DS10 during the first 2 weeks of the quake, which they calculate as a short-term linear rate of about 1 mm/day, and their interpretations of the data are similar to ours (Wdowinski *et al.*, unpublished manuscript). Postseismic strain relaxation was recorded also at the Pinyon Flat Observatory, about 70 km south of the Landers earthquake epicenter (Wyatt *et al.*, 1994), where strainmeter observations are fit to an exponential relaxation model with a 5-day relaxation time. This observation may not conflict with our 34-day relaxation time estimate, since we did not record at the field sites the first 36 h of the crustal deformation after the earthquake as did Wyatt *et al.* (1994). Additionally, they speculated that these differences in time behavior may be caused by more than one process.

The reduced postfit standard rms for model A is 2.63, indicating that a significant portion of the data cannot be explained by the model. There are numerous possible sources for the misfit, such as errors in estimating the steady aseismic motions, relaxation occurring in a blind horizontal viscous layer in the upper mantle, simplified representation of a 3D heterogenous rupture zone by a fault patch model, relaxation with more than one time constant, and contribution from small faults or asperities

Table 5
Model Statistics

Model	Fault Tested	χ^2	Resolution	F Test†
A	—	121.4	17.2	—
B	Barstow	194.0	15.7	99%
C	2 East–West Lobes	144.3	16.0	90%
D	Pisgah	118.9	16.5	51%‡
F	Banning	141.8	15.7	84%
I	upper layer only	348.4	15.1	99%
J	lower layer only	456.3	10.6	99%

*χ^2 data residual χ^2.
†F Test: confidence test against model A.
‡Total residual χ^2 used for F test.

not modeled in this study. For the last possibility, for example, significant misfit at station GODW could be explained by right-lateral slip along a portion of the Pisgah fault south of the Pisgah aftershock zone, and misfit at station 6052 could be caused by slip along the Lenwood fault. Despite so many uncertainties, however, our model has explained 90% of the variance of the prefit data, suggesting that relaxation along or around the faults is the major contributor to the postseismic motions.

We test also models with uniform depth variations for both the upper and lower layers. The data are unable to resolve the depths of the creeping patches well. The best estimates of the depths of the two-layer fault patches are 10 and 35 km, although a variation of a couple of kilometers for the depth of the upper layer, or a 10-km depth variation for the lower layer, would not change the quality of the fit by very much.

For the resolved slip along the faults, the Barstow patch offers the largest displacement, 249 ± 53 mm, which is probably driven by heightened static stress changes which reached a maximum in this area, according to calculations by Stein *et al.* (1992). Large displacement along the main rupture zone is concentrated at the southern Johnson Valley, Eureka Peak, and the northern Joshua Tree areas, with a maximum slip of 156 ± 50 mm. It is perplexing to see a big contrast in slip between the northern and southern Johnson Valley patches in the first layer: 76 mm of a left-lateral slip versus 123 mm of right-lateral slip. This could be interpreted as overshoot of the northern patch during the main rupture, evidenced by a geologically observed local maximum surface slip there (Hart *et al.*, 1993), and as a catch-up of the southern patch following the mainshock, although other explanations cannot be ruled out. One of them is the complexity of the rupture zone, as evidenced by radar interferometry data (Massonnet *et al.*, 1993). Geodetic inversion techniques are sensitive to the locations of nodal points when the stations are very close to a complex rupture, as is station PAXU.

The overall high slip concentration can be compared with the postseismic results of near-field trilateration surveys by Sylvester (1993). He found virtually no near-field postseismic slip along the northern part of the main rupture zone. Near-field slip along the southern part measured 9 mm at a site within our southern Johnson Valley patch and 40 mm at a site within our Eureka Peak patch. This overall pattern of near-field postseismic surface slip along the rupture zone, with measurable slip increasing southerly, is consistent with our results. Two patches along the Banning fault yield fairly significant right-lateral slip, 119 ± 37 and 100 ± 86 mm, respectively. The third patch favors a slight left-lateral slip, but it is not statistically significant. We have 63 to 96-mm slip along the lower patches of the Big Bear fault, and up to 100 mm along the patches of the two east–west aftershock lobes east of the Camp Rock fault.

If we convert the slip along the faults into moments (Table 6), we find that the total postseismic moment release 1.7×10^{19} N-m is about 15% of the co-seismic moment release of 1.1×10^{20} N-m (Kanamori *et al.*, 1992). The postseismic moment release along the mainshock rupture zone alone amounts to about 6% of the co-seismic moment release. It seems that areas outside the mainshock rupture zone contribute significantly to the total postseismic moment release. This observation suggests that the Mojave Shear Zone is a highly fractured, low strength structure, where a stress disturbance can cause fractures in a broad region. Significant sympathetic slip along neighboring faults accompanying the Landers earthquake (Hart *et al.*, 1993) supports this conjecture. This is also consistent with the previous geological and geodetic studies that the secular deformation spans a broad shear zone (Dokka and Travis, 1990; Sauber *et al.*, 1986; Savage *et al.*, 1990), indicating that a wide range of faults in the deformation zone were near critical failure.

Significant cumulative aftershock seismic moment release has occurred at the Barstow aftershock zone, amounting to about 8.2×10^{16} N-m from 28 June 1992 to 1 June 1993. This number is calculated from an edited earthquake catalog by the USGS/Caltech seismological office (Susan Hough and Lisa Wald, personal comm.), with about one-third of the earthquakes, including most of the larger ones, compiled. The total aftershock moment release is likely to be on the order of 10^{17} N-m. Thus, the aftershock moment release accounts for only a few percent of the total postseismic moment release.

The ratios of the geodetically inverted postseismic moment to the aftershock moment are about 4.6 along both the Camp Rock–Joshua Tree seismic zone and along the Pisgah aftershock zone, and 6.4 along the Big Bear fault. Such ratios are small compared to other fault patches in this study. A number of magnitude 5 aftershocks have occurred along the faults from Eureka Peak to Joshua Tree, and along the Pisgah aftershock zone and the Big Bear fault. These low ratios possibly reflect the birth of young faults in the regions, accompanied by heavy aftershock seismicity.

Table 6
Fault Postseismic Moment Release

Fault Patch	Geodetic Moment (10^{18} N-m)		Seismic Moment (10^{18} N-m)
	Upper Layer	Lower Layer	
Barstow	0.26	3.60	0.082
2 E–W Lobes	0.31	1.65	0.044
Camp Rock–Joshua Tree	0.93	5.50	1.40
Big Bear	0.09	1.71	0.28
Banning	—	2.85	0.003
Pisgah	0.16	0.42	0.16
Total	1.75	15.7	2.0

Within the area of the Banning fault and the San Bernardino Mountain segment of the San Andreas fault, accumulated aftershock seismic moment release is about 3×10^{15} N-m (Susan Hough and Lisa Wald, personal comm.). Taking the undocumented events into account, the release might be as large as 10^{16} N-m. This number is 2 to 3 orders of magnitude less than the geodetically estimated moment release. This observation suggests that the Banning fault has slipped aseismically following the main event, although given the limited geodetic data, it is difficult to resolve the horizontal extent and the depth range of the slip.

If we evaluate separately the geodetic moments from the upper and lower layers, and compare them with the seismic moments along the patches, we find that although the comparison along each segment may vary, the total geodetic moment from the upper layer only is about the same as the total seismic moment. This observation confirms that the afterslip observed in the upper 10 km of the faults took place seismically, while the bulk of the afterslip happened aseismically below the seismogenic zone. It is interesting, though not particularly conclusive, that for the power-law model of afterslip, the exponent p is consistent with values determined from aftershock sequences (Reasenberg and Jones, 1989).

The general pattern of postseismic displacement resembles that of the co-seismic geodetic displacements (Ge *et al.*, 1993; Hudnut *et al.*, 1994; Freymueller *et al.*, 1994), in that it can be mostly explained by slip with the same sense of motion on the same faults. However, the co-seismic displacements can be explained by fault slip shallower than 10 km, while the postseismic cannot. The postseismic displacements decay much more slowly with distance than do the co-seismic displacements, suggesting the interpretation that the postseismic displacement is caused primarily by delayed slip on the downward extension of the rupture surface. Perhaps rapid, episodic slip and slower viscous or plastic slip collaborate to reduce the shear stress across a fault, with the proportional share determined by the rate of viscous deformation. The viscous deformation should be faster at depth where the temperature is higher. It may also be faster where the stress is high, at the margins of the rupture zone and possibly at local sites within the rupture surface. To speculate further, this viscous or plastic stress release may locally increase the stress where the inelastic process cannot keep up with surrounding regions. Thus, inelastic yielding both within and around the rupture surface may control the temporal pattern of aftershock occurrence.

Conclusions

Using the GPS technique, we have monitored postseismic deformation following the Landers earthquake. Our results demonstrate that the postseismic deformation is significant both at the rupture zone and at neighboring areas activated by that earthquake. The postseismic deformation can be modeled as afterslip along faults activated by the mainshock. The major contribution comes from a presumably viscous layer beneath the seismogenic zone. The geodetically estimated postseismic moment release is about 15% of the co-seismic moment release. The total geodetically determined postseismic moment release along faults in the upper 10-km depth is about the same as the seismic aftershock moment release, suggesting brittle afterslip above that depth and ductile slip below. We estimate the relaxation time for an exponential decay model to be about 34 days, with logarithmic relaxation and power-law relaxation models being equally valid. We find that the relaxation deformation is significant at the Barstow aftershock zone, the southern Johnson Valley fault, Eureka Peak fault, northern Joshua Tree fault, and possibly the Banning fault.

Acknowledgments

We thank Duncan Agnew, Richard Snay, Jeff Freymueller, Ken Hudnut, Ken Hurst, and Shawn Larson for helping to sketch the initial survey response plan. Olga Bernaldo, Bob Ge, Jeff Genrich, J. Hanson, Weishi Huang, Hadley Johnson, Tania Levshina, Greg Lyzenga, Mark Martins, Norman Meek, Chris Mills, Dave Potter, Manuel Ramirez, Gene Ratcliffe, Steve Salyards, Jennifer Scott, Victor Vazquez, and Rich Zitola contributed greatly by collecting GPS data in the field on short notice under difficult conditions. Additionally, we thank James Stowell for swiftly shipping GPS receivers to the field after the quake; UNAVCO engineers Brennan O'Neill and Tony Stephens for their field technical support; and Ken Hudnut and Rob Reilinger for providing site descriptions. We are grateful to Karl Gross and the USGS field crew; A. Lindsay, C. Smith, and surveyors of NGS field party G-02; Lawrence Fenske and surveyors of Caltrans; Mike Raihle and surveyors of San Bernardino County; William Young, Gerald Doyle, and surveyors of Riverside County, among many others. This work has been supported by the National Science Foundation (grants EAR 86-18393 and EAR 92-08447), the United States Geological Survey (USDI grant 14-08-001-G1956 and Cooperative Agreement 14-08-00001-A0899), National Aeronautics and Space Administration (grant NAG 5-1917), and the Southern California Earthquake Center (P.O. 566259). Southern California Earthquake Center publication 104.

References

Beutler, G. and E. Brockmann, Editors (1993). *Proc. of the 1993 IGS Workshop, Int. Assoc. of Geodesy*, Druckerei der Universitat Bern, Bern, Switzerland.

Bock, Y., S. A. Gourevitch, C. C. Counselman III, R. W. King, and R. I. Abbot (1986). Interferometric analysis of GPS phase observation, *Manuscr. Geod.* **11**, 282–288.

Dokka, R. K. and C. J. Travis (1990). Role of the eastern California shear zone in accommodating Pacific–North American plate motion, *Geophys. Res. Lett.* **17**, 1323–1326.

Dong, D. N. and Y. Bock (1989). Global Positioning System network analysis with phase ambiguity resolution applied to crustal deformation studies in California, *J. Geophys. Res.* **94**, 3946–3966.

Feigl, K. L. (1991). Geodetic measurement of tectonic deformation in central California, *Ph.D Thesis*, Massachusetts Institute of Technology, Cambridge, 223 pp.

Feigl, K. L., D. C. Agnew, Y. Bock, D. Dong, A. Donnellan, B. H. Hager, T. A. Herring, D. D. Jackson, T. H. Jordan, R. W. King, S. Larsen, K. M. Larson, M. H. Murray, Z. Shen, and F. H. Webb (1993). Space geodetic measurement of crustal deformation in central and southern California, 1984–1992, *J. Geophys. Res.* **98**, 21677–21712.

Fitch, T. J. and C. H. Scholz (1971). Mechanism of underthrusting in southwest Japan: a model of convergent plate interactions, *J. Geophys. Res.* **76**, 7260–7292.

Freymueller, J. T., N. E. King, and P. Segall (1994). The coseismic slip distribution of the Landers Earthquake, *Bull. Seism. Soc. Am.* **84**, no. 3, 646–659.

Ge, X. B., Z. Shen, Y. Feng, and D. D. Jackson (1993). Coseismic fault slips in the 1992 Landers and Big Bear earthquakes determined by GPS, *EOS* **74**, no. 43, 429.

Hart, E. W., W. A. Bryant, and J. A. Treiman (1993). Surface faulting associated with the June 1992 Landers Earthquakes, California, *Calif. Geol.* **46**, no. 1, 10–16.

Hauksson, E., L. M. Jones, K. Hutton, and D. Eberhart-Philips (1993). The 1992 Landers earthquake sequence: seismological observations, *J. Geophys. Res.* **98**, 19835–19858.

Hudnut, K. W., Y. Bock, M. Cline, P. Fang, Y. Feng, J. Freymueller, X. Ge, W. K. Gross, D. Jackson, M. Kim, N. E. King, J. Langbein, S. C. Larsen, M. Lisowski, Z.-K. Shen, J. Svarc, and J. Zhang (1994). Co-Seismic Displacements of the 1992 Landers Earthquake Sequences, *Bull. Seism. Soc. Am.* **84**, no. 3, 625–645.

IERS (1992). Annual report for 1991, IERS Central Bureau, Observatoire de Paris.

Jackson, D. D. (1979). The use of a priori data to resolve the nonuniqueness in linear inversion, *Geophys. J. R. Astr. Soc.* **57**, 137–157.

Jackson, D. D. and M. Matsu'ura (1985). A Bayesian approach to nonlinear inversion, *J. Geophys. Res.* **90**, 581–591.

Jaeger, J. C. and N. G. W. Cook (1979). *Fundamentals of Rock Mechanics*, Third Ed., Chapman and Hall, London.

Kanamori, H., H.-K. Thio, D. Dreger, E. Hauksson, and T. Heaton (1992). Initial investigation of the Landers, California, earthquake of 28 June 1992 using TERRAscope, *Geophys. Res. Lett.* **19**, 2267–2270.

King, R. W. and Y. Bock (1993). *Documentation for the MIT GPS Analysis Software: GAMIT*, Massachusetts Institute of Technology, Cambridge.

Li, V. C. and J. R. Rice (1987). Crustal deformation in great California earthquake cycles, *J. Geophys. Res.* **92**, 11533–11551.

Massonnet, D., M. Rossi, C. Carmona, F. Adragna, G. Peltzer, K. Feigl, and T. Rabaute (1993). The displacement field of the Landers earthquake mapped by radar interferometry, *Nature* **364**, 138–142.

Matsu'ura, M., D. D. Jackson, and A. Cheng (1986). Dislocation model for aseismic crustal deformation at Hollister, California, *J. Geophys. Res.* **91**, 12661–12674.

Nur, A. and G. Mavko (1974). Post-seismic viscoelastic rebound, *Science* **183**, 204–206.

Okada, A. and T. Nagata (1953). Land deformation of the neighborhood of Muroto Point after the Nankaido great earthquake in 1946, *Bull. Earthquake Res. Inst. Tokyo Univ.* **31**, 169–177.

Reasenberg, P. A. and L. M. Jones (1989). Earthquake hazard after a mainshock in California, *Science* **243**, 1173–1176.

Reilinger, R. (1986). Evidence for postseismic viscoelastic relaxation following the 1959 $M = 7.5$ Hebgen Lake, Montana, earthquake, *J. Geophys. Res.* **91**, 9488–9494.

Rundle, J. B. and D. D. Jackson (1977). A viscoelastic relaxation model for postseismic deformation from the San Francisco earthquake of 1906, *Pageoph* **115**, 401–411.

Sauber, J., W. Thatcher, and S. Solomon (1986). Geodetic measurement of deformation in the central Mojave Dessert, California, *J. Geophys. Res.* **91**, 12683–12693.

Savage, J. C. (1990). Equivalent strike-slip earthquake cycles in half-space and lithosphere-asthenosphere earth models, *J. Geophys. Res.* **95**, 4873–4879.

Savage, J. C., M. Lisowski, and W. H. Prescott (1990). An apparent shear zone trending north-northwest across the Mojave Dessert into Owens Valley, eastern California, *Geophys. Res. Lett.* **17**, 2113–2116.

Savage, J. C. and W. H. Prescott (1978). Asthenosphere readjustment and the earthquake cycle, *J. Geophys. Res.* **83**, 3369–3376.

Savage, J. C., W. H. Prescott, and M. Lisowski (1987). Deformation along the San Andreas fault 1982–1986 as indicated by frequent geodolite measurements, *J. Geophys. Res.* **92**, 4785–4797.

Schaffrin, B. and Y. Bock (1988). A unified scheme for processing GPS phase observations, *Bull. Geod.* **62**, 142–160.

Sieh, K., L. Jones, E. Hauksson, K. Hudnut, D. Eberhart-Phillips, T. Heaton, S. Hough, K. Hutton, H. Kanamori, A. Lilje, S. Lindvall, S. F. McGill, J. Mori, C. Rubin, J. A. Spotila, J. Stock, H.-K. Thio, J. Treiman, B. Wernicke, and J. Zachariasen (1993). Near-field investigations of the Landers earthquake sequence, April to July 1992, *Science* **260**, 171–176.

Stein, R. S., G. L. P. King, and J. Lin (1992). Change in failure stress on the southern San Andreas fault system caused by the 1992 magnitude = 7.4 Landers earthquake, *Science* **258**, 1328–1332.

Stein, R. S. and M. Lisowski (1983). The 1979 Homestead valley earthquake sequence, California: control of aftershocks and postseismic deformation, *J. Geophys. Res.* **88**, 6477–6490.

Sylvester, A. G. (1993). Investigation of nearfield postseismic slip following the M_w 7.3 Landers earthquake sequence of 28 June 1992, California, *Geophys. Res. Lett.* **20**, 1079–1082.

Thatcher, W. (1983). Nonlinear strain buildup and the earthquake cycle on the San Andreas fault, *J. Geophys. Res.* **88**, 5893–5902.

Tse, S. T. and J. R. Rice (1986). Crustal earthquake instability in relation to the depth variation of frictional slip properties, *J. Geophys. Res.* **91**, 9452–9472.

Wdowinski, S., Y. Bock, P. Fang, J. F. Genrich, D. C. Agnew, and F. K. Wyatt (1992). Detection of coseismic and postseismic surface displacement, *EOS* **73**, no. 43, 364.

Wyatt, F. K., D. C. Agnew, and M. Gladwin (1994). Continuous measurements of crustal deformation for the 1992 Landers earthquake sequence, *Bull. Seism. Soc. Am.* **84**, no. 3, 768–779.

3806 Geology
Department of Earth and Space Sciences
University of California
Los Angeles, California 90024-1567
(Z.S., D.D.J., Y.F., M.C., M.K.)

I.G.P.P.
Scripps Institution of Oceanography
University of California, San Diego
La Jolla, California 92093
(P.F., Y.B.)

Manuscript received 2 August 1993.